Stress-dependent Magnetic Flux Leakage: Finite Element Modelling simulations vs. Experiment

Yujue Wang[1], Yevgen Melikhov[1], Turgut Meydan[1], Zengchong Yang[2], Donghang Wu[2], Bin Wu[2], Cunfu He[2], Xiucheng Liu[2*]

1 Wolfson Centre for Magnetics, School of Engineering, Cardiff University, CF24 3AA, UK
2 College of Mechanical Engineering and Applied Electronics Technology, Beijing University of Technology, P.R. China
**Corresponding author's E-mail: xiuchliu@bjut.edu.cn*

Abstract: Assessing the effect of defect induced stresses on magnetic flux leakage (MFL) signals is a complicated task due to nonlinear magnetomechanical coupling. To facilitate the analysis, a multi-physics finite elemental simulation model is proposed based on magnetomechanical theory. The model works by quasi-statically computing the stress distribution in the specimen, which is then inherited to solve the nonlinear magnetic problem dynamically. The converged solution allows identification and extraction of the MFL signal induced by the defect along the sensor scanning line. Experiments are conducted on an AISI 1045 steel specimen, i.e. a dog-bone shaped rod with a cylindrical square-notch defect. The experiments confirm the validity of the proposed model that predicted a linear dependency of the peak-to-peak amplitude of the normalized MFL signal on applied stress. Besides identifying the effect of stress on the induced MFL signal, the proposed model is also suitable for solving the inverse problem of sizing the defects when stress is involved.

Keywords: Magnetic flux leakage, Magnetomechanics, Jiles-Atherton model, Non-destructive testing, Finite element method, Multiphysics numerical simulation

1. Introduction

The magnetic flux leakage (MFL) method is commonly utilized to non-destructively evaluate the damage in ferromagnetic materials due to its reliability, high efficiency and cost-saving. In MFL applications, specimens are magnetized and the leakage flux occurring near geometric discontinuities is detected by MFL sensors [1, 2]. The detected MFL signals are then used inversely to evaluate the sizes of defects. The inverse problem involves many challenges. For example, stress, which is a common condition, affects the MFL signal considerably. If being neglected, the inverse problem will lead to a significant error in defect sizing. The experimental results of Mandal *et al.* [3, 4] showed that circumferential hoop stress generated by in-service pipelines could alter the peak values of MFL signals by more than 40%. Wang *et al.* [5] found that tensile stress of 100MPa applied to a dog-bone specimen with a cylindrical through-hole could cause an increase of 24% in peak-to-peak amplitude of the MFL signal. Therefore, to evaluate the sizes of defects accurately, it is necessary to consider the effects of stress on the MFL signals.

To accurately evaluate the effect of stress on the MFL signal, previous work has attempted to mathematically fit experimental results with analytical outcomes. Mandal *et al.* [4] used analytical models of Zatsepin-Shcherbinin [6] and Edwards-Palmer [7] to fit experimental data under different stresses by altering the densities of magnetic charges. However, stress as an external variable was not considered in their models, and the values of the densities were changed artificially. Hence, this method could be used qualitatively, rather than quantitatively, to size defects.

Wang *et al.* [5] proposed the improved dipole model by introducing the stress-dependent Jiles-Atherton (J-A) model into the traditional dipole model. The improved dipole model could accurately predict the effect of stress on the MFL signal induced by a defect with regular geometry. However, for non-regular geometries the model can no longer provide an analytical solution due to the difficulty in calculating the stress concentration and the demagnetizing factor around the defect. The analytical model also only considers the stress distribution along the wall of the defect rather than over the whole stress concentration area. In addition, even small stresses applied to a defect with a regular or simple geometry may transform the geometry of that defect into a more complex one.

Compared with the analytical models, the finite element method (FEM) can compete with the former due to its flexibility in computation, and it can also give the overall perspective of simulation. A number of attempts have been made to model MFL and stress-dependent MFL by using FEM. The pioneering finite element modelling of the MFL field by Hwang and Lord [8] paved the way for the numerical analysis of defect-induced MFL signals. With improvements in computational capabilities, significant progress has been made in this area by considering non-linear material properties [9-11] and coupling them with stress [12-15]. Ivanov *et al.* [12] incorporated stress distributions into the magnetic FEM model by varying the permeability in the region under stress. Babbar *et al.* [13, 14] introduced stress information into the magnetic FEM model by adjusting the permeability variable. In other studies, adjustments of simulation results fitted to experimental ones were performed by changing one or more magnetic properties, which may not correspond to the reality [9-11]. FEM simulations of stress-induced MFL signals are more difficult to achieve compared to situations without stress since the magnetic permeability, magnetization and demagnetization are stress dependent as well as being nonlinear functions of the applied field. Zhong *et al.* [15] built an FEM model that coupled stress concentration in the reversible magnetization region. This could be used to qualitatively evaluate defects rather than quantitatively identify defects due to relatively large errors.

In order to solve the coupled magnetomechanical problem in defect reconstruction from MFL signals, a multiphysics FEM model is proposed in this paper by interlinking the physics of mechanics and magnetics. To test our model, COMSOL Multiphysics software[16] is chosen using both its solid mechanics and low-frequency electromagnetic (AC/DC) modules. The solid mechanics module is used to calculate the stress distribution within an AISI 1045 steel specimen with particular attention paid to the circumferential square-notch defect on the rod. The electromagnetic module is employed to simulate magnetic field under stress, via the Jiles-Atherton-Sablik (J-A-S) theory [17, 18]. Experimental tests are conducted to verify the feasibility of the proposed FEM model. Finally, a quantitative prediction on the effect of stress on the defect-induced MFL signal is achieved.

This paper is organized as follows. In Section 2, the multiphysics finite element model is proposed and explained along with the simulation results on a case study. In Section 3, the details about the verification experiments including the specimen tempered procedure and the configuration of the MFL sensor are explained. Both the performance and limitations of the proposed FEM model are discussed in Section 4. Finally, the major findings of this study are discussed in Section 5.

2. Magneto-mechanical simulation algorithm and its application to a Case Study

This paper aims at proposing a universal finite element method for revealing the relation between stress and the MFL signal due to a defect with any geometry. In the case of such defect, which is hard to describe the stress distribution analytically, the dependence of magnetic hysteretic properties on stress makes the problem even more complex. Therefore, the finite element method is employed to simulate the real physical phenomenon.

2.1 Step 1: Solid mechanics module

In order to simplify the formulation and presentation of the theory, a two-dimensional (2D) axisymmetric system is chosen, with axisymmetric sample and defect geometries. The theory for three-dimensional systems that lack symmetry can also be formulated in a similar manner. In addition, to the mechanics study, quasi-static conditions are assumed, i.e. negligible changes in stress over the time period required to perform magnetic measurements. The simulation also deals with elastic rather than plastic stress to avoid nonconvergence of iteration due to strong non-linearity in magnetic behaviour[19].

With these constraints in mind, and assuming that the ferromagnetic material is a mechanically isotropic medium, the following equilibrium equation describes the mechanical problem:

$$\nabla\boldsymbol{\sigma} + \mathbf{F} = \mathbf{0} \tag{1}$$

where $\boldsymbol{\sigma}$ is the stress tensor and $\mathbf{F}$ is the body force. The constitutive relation:

$$\boldsymbol{\sigma} = \mathbf{D}\boldsymbol{\varepsilon} \tag{2}$$

is used, where $\mathbf{D}$ is the elasticity tensor of the material and $\boldsymbol{\varepsilon}$ is the strain tensor.

Together with the geometrical constraints of the system, a solution to the mechanical problem is obtained using an FEM approach implemented in the solid mechanics module of COMSOL. The results of these solid mechanics simulations (i.e., distribution of stress in the ferromagnetic structure) are stored and passed as inputs for the magnetic simulations.

2.2 Step 2: Low-frequency electromagnetic module

The solid mechanics simulations are performed under quasi-static conditions. While the magnetic simulations have to be dynamic due to the hysteresis loop where one-to-one correspondence between states of magnetization and the applied magnetic field is absent. A time-dependent magnetic field $\boldsymbol{H}$ can uniquely determine the magnetization $\boldsymbol{M}$ value at a particular moment of time by employing hysteresis model. Besides, the ferromagnetic material of the specimen is chosen to be magnetically isotropic following the Jiles-Atherton-Sablik dynamical magnetomechanical hysteretic theory.

A typical algorithm to solve a time-dependent magnetomechanical problem is as follows [20]:

(1) Magnetic field ($\mathbf{H}$) is set as a sinusoidal (or triangular) function varying with time (t). Generally, this magnetic field can be generated by feeding a sinusoidal alternating current into excitation coils. In this paper, the first quarter period of the sinusoidal current is fed into Helmholtz coils to excite magnetic field, and then maintaining the current at the peak value so that the magnetic field and magnetization remains unchanged in subsequent calculations, as shown in Fig.1a. $\mathbf{H}(t)$, $\mathbf{B}(t)$ and $\mathbf{H}_e(t\text{-}\Delta t)$ start from $\mathbf{H}(0)$, $\mathbf{B}(0)$, $\mathbf{H}_e(0)$ and then are updated after every algorithmic loop.

(2) For the given actual time step magnetic field $\mathbf{H}(t+\Delta t)$, the magnetization $\mathbf{M}(t)$ and increment of magnetic field $d\mathbf{H}(t)$ can be calculated by

$$\mathbf{M}(t) = \mathbf{B}(t)/\mu_0 - \mathbf{H}(t) \tag{3}$$

$$d\mathbf{H} = \mathbf{H}(t + \Delta t) - \mathbf{H}(t) \tag{4}$$

where μ_0 is the permeability of free space. Then the effective magnetic field $\mathbf{H_e}(t)$ [21] and the increment of effective field $d\mathbf{H_e}(t)$ are computed by

$$\mathbf{H}_e = \mathbf{H}(t) + (\boldsymbol{\alpha} + \frac{3\mathbf{b}\boldsymbol{\sigma}}{\mu_0}) \cdot \mathbf{M}(t) = \mathbf{H}(t) + \tilde{\boldsymbol{\alpha}} \cdot \mathbf{M}(t) \tag{5}$$

$$d\mathbf{H}_e = \mathbf{H}_e(t) - \mathbf{H}_e(t - \Delta t) \tag{6}$$

where $\boldsymbol{\alpha}$ quantifies the amount of domain coupling, $\boldsymbol{\sigma}$ is the stress tensor, the coefficient $\mathbf{b}$ is a function of magnetostriction ($\boldsymbol{\lambda}$) and magnetization ($\mathbf{M}$), and $\tilde{\boldsymbol{\alpha}}$ is the total interdomain coupling parameter.

(3) According to the J-A model [17, 20-22], the differential magnetization with respect to the magnetic field can be expressed as

$$\frac{d\mathbf{M}}{d\mathbf{H}} = \frac{\frac{\boldsymbol{\chi}_f}{|\boldsymbol{\chi}_f|}\cdot\boldsymbol{\chi}_f + \mathbf{c}\cdot\frac{d\mathbf{M}_{an}}{d\mathbf{H}_e}}{1-\tilde{\boldsymbol{\alpha}}\left[\frac{\boldsymbol{\chi}_f}{|\boldsymbol{\chi}_f|}\cdot\boldsymbol{\chi}_f + c\cdot\frac{d\mathbf{M}_{an}}{d\mathbf{H}_e}\right]} \tag{7}$$

where $\mathbf{c}$ is the reversibility coefficient, $\mathbf{M}_{an}$ is an anhysteretic magnetization, which is given by the Langevin function in the case of an isotropic material [23]:

$$\mathbf{M}_{an}(t) = \mathbf{M}_s \left[\coth\frac{\mathbf{H}_e(t)}{\mathbf{a}} - \frac{\mathbf{a}}{\mathbf{H}_e(t)}\right] \tag{8}$$

and $\boldsymbol{\chi}_f = (\mathbf{M}_{an} - \mathbf{M})/\mathbf{k}$, where $\mathbf{k}$ is the pinning coefficient. Equation (7) holds true with the condition $\boldsymbol{\chi}_f \cdot d\mathbf{H}_e(t) > 0$; otherwise, Equation (7) changes to:

$$\frac{d\mathbf{M}}{d\mathbf{H}} = \frac{\mathbf{c}\cdot\frac{d\mathbf{M}_{an}}{d\mathbf{H}_e}}{1-\tilde{\alpha}\mathbf{c}\cdot\frac{d\mathbf{M}_{an}}{d\mathbf{H}_e}} \tag{9}$$

(4) Based on the computed results in previous steps, magnetization **M**, magnetic induction **B** and effective field $\mathbf{H}_e$ are updated by

$$\mathbf{M}(t+\Delta t) = \mathbf{M}(t) + \frac{d\mathbf{M}}{d\mathbf{H}}\cdot d\mathbf{H} \tag{10}$$

$$\mathbf{B}(t+\Delta t) = \mu_0[\mathbf{H}(t+\Delta t) + \mathbf{M}(t+\Delta t)] \tag{11}$$

$$\mathbf{H}_e(t-\Delta t) = \mathbf{H}_e(t) \tag{12}$$

This data is inputted into the next computing loop repeating the algorithmic steps (2)-(5). These procedures are not finished until the last time step is completed. In this case study, the initial hysteresis curve is used to reduce simulation time by feeding the first quarter period of the sinusoidal current into the excitation coils (see Fig.1). It should be added that this algorithm can obtain all magnetization states on the hysteresis loop by feeding the complete alternating current waveform into the excitation coils. For example, it will obtain a whole hysteresis loop by using an alternating current cycle of one and a quarter periods.

Before simulation, identification of the key parameters for the model is required. To simplify the expressions, the tensors of the J-A parameters are expressed as scalar values since the specimen is set as an isotropic material, for example $\mathbf{M}_s = \begin{bmatrix} M_s & 0 & 0 \\ 0 & M_s & 0 \\ 0 & 0 & M_s \end{bmatrix}$ is simplified as M_s.

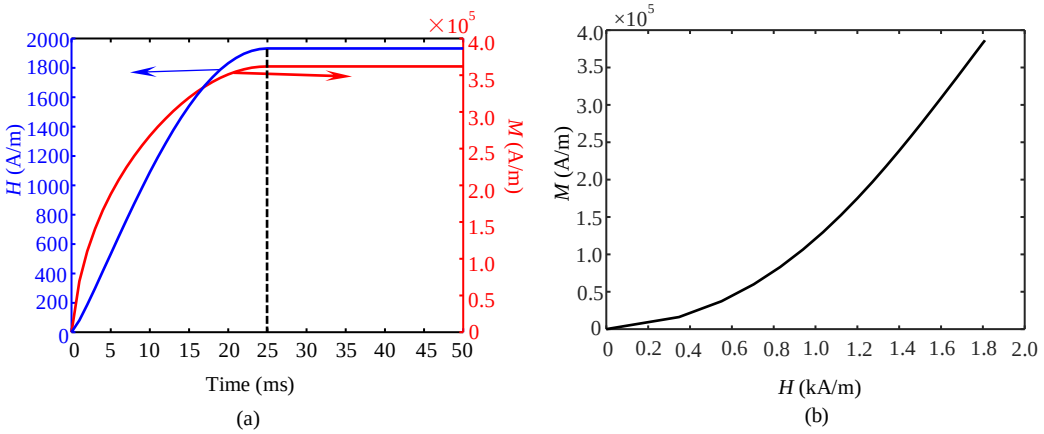

Fig. 1 (a) The magnetic field (*H*) and magnetization (*M*) variations with time extracted from a point inside a specimen without defect, (b) the *M*-*H* part of the hysteresis curve corresponding to (a).

2.3 Case study: Dog-bone like rod of 1045 steel with a square-notch defect

Similar to Ref.[5], where a cylindrical through-hole on a dog-bone shaped plate specimen was used to verify the stress-dependent dipole model, in this paper, a dog-bone shaped rod (shown in Fig.2a) with a circumferential square-notch defect is studied to reveal the relation between stress and MFL signal. In case of such a defect, it is hard to describe the stress distribution around the defect analytically.

The solid mechanics is simulated using COMSOL Multiphysics 5.2a. As shown in Fig.2b, a 2-D axisymmetric model in the *r*-*z* plane is built according to the geometric structure of the dog-bone shaped

rod specimen shown in Fig.2a and the sensor designed in our previous research [24]. The geometric parameters of the specimen and the defect are listed in Table 1. In the first simulation step, when the tensile stress is applied, the mechanical problem is solved in the mechanics module. The free triangular mesh using an adaptive algorithm is applied to the specimen with a predefined extremely fine element size. Element sizes are set to less than 0.01 mm around the defect adding extremely fine auxiliary lines along the periphery of defect to obtain an accurate stress distribution around the defect.

In the mechanics module, one of the test specimen's ends is fixed while the other one is subject to a force that generates stresses in the "reduced" section (as shown in Fig.2a). The force values are chosen such that the average stress values away from the defect varied from 0 MPa to 100 MPa in 10 MPa intervals. The stress distribution in the region near the defect is complex due to shape effects leading to the stress concentration, and is computed by the stationary solver. The typical result of the applied tensile stress (100 MPa) is illustrated in Fig.2c. In the region that is far from the defect, the stress distributes nearly uniformly, while in the vicinity of the defect the stress varies sharply, especially at the bottom of the square-notch defect. The stress along a cut-line of [(6.5, −0.5), (7.0, -0.5)] is extracted to evaluate the variation of stress along the wall of the defect. The curve of the stress on the cut-line is plotted in Fig.2d. It can be seen that the stress decreases to zero rapidly and then increases slowly towards zero after reaching a minimum at about -13 MPa. Obviously, compared with the stress distribution around the cylinder defect in Ref. [5], the stress along the vicinity of the defect is hard to describe mathematically justifying the choice of the FEM simulations. After applying the stress, the square-notch defect, which initially had a regular shape, has acquired a complex geometry as shown in Fig.2c.

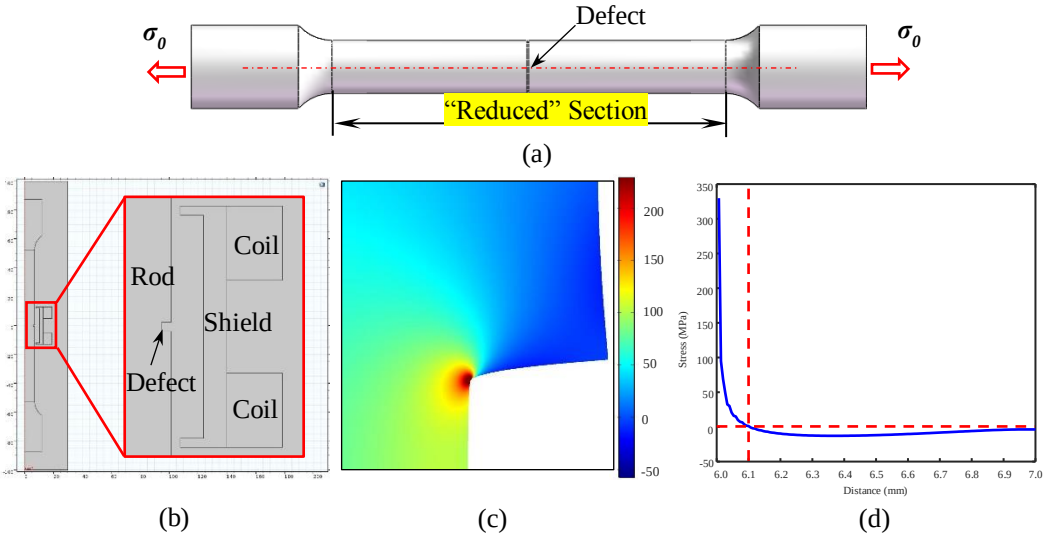

Fig. 2 Solid mechanical analysis of a dog-bone shaped rod with a square-notch defect. (a) The tensioned test specimen, (b) the 2-D axisymmetric model, (c) the calculated result of stress distribution around the defect (notice the change of shape of the specimen near the defect), and (d) stress distribution curve extracted along an edge of defect.

Table 1. The geometric parameters of the modelled specimen

Geometric Parameters	Length of specimen	Length of the central part	Depth of the defect	Width of the defect	Radius of the ends	Radius of the central part
Sizes (mm)	175	105	1	1	12	7

The results of solid mechanics module simulations under different stresses are stored in solver sets with the stress values which are used as the inputs of the AC/DC module.

The test specimen made of 1045 steel is used in this case. The five J-A parameters of 0.4%wt carbon steel fitted by nonlinear optimization algorithm [25] are substituted into the finite elemental model to simulate the hysteresis curve approximately. Mierczak *et al.* [26, 27] fitted the average λ vs M values using a parabolic function to quantitatively evaluate the effect of stress on magnetic Barkhausen noise (MBN) emissions. The linear stress-based MBN model corresponding to the experimental results with high coefficients of determination ($R^2 \geq 0.9827$) [27] validated the feasibility of their proposed model. Therefore, based on the previously measured λ vs M curve [17], the coefficient b is determined as 2.2×10^{-18} (m^2/A^2) by the parabolic fitting of the λ vs M curve. In the following experiments the input current is set at 3 A, and since the diameter of the wire is 0.35 mm, the input current density in the model is set at 30 A/mm^2 (see Table 2 for the parameter values of the magnetomechnical model).

Table 2. The J-A model parameters for 0.4wt% carbon steel

J-A Parameters	Value	Obtained from
Saturation magnetization, M_s	1.5755×10^6 (A/m)	
Domain density, a	1408.1 (A/m)	
Coupling factor, α	0.0024	Ref.[25]
Pinning parameter, k	2356.5 (A/m)	
Reversibility parameter, c	0.0382	
Magnetostriction coefficient, b	2.2×10^{-18} (m^2/A^2)	Ref.[17], [25], [26]
Input current density, J_0	30 (A/mm^2)	Experiment

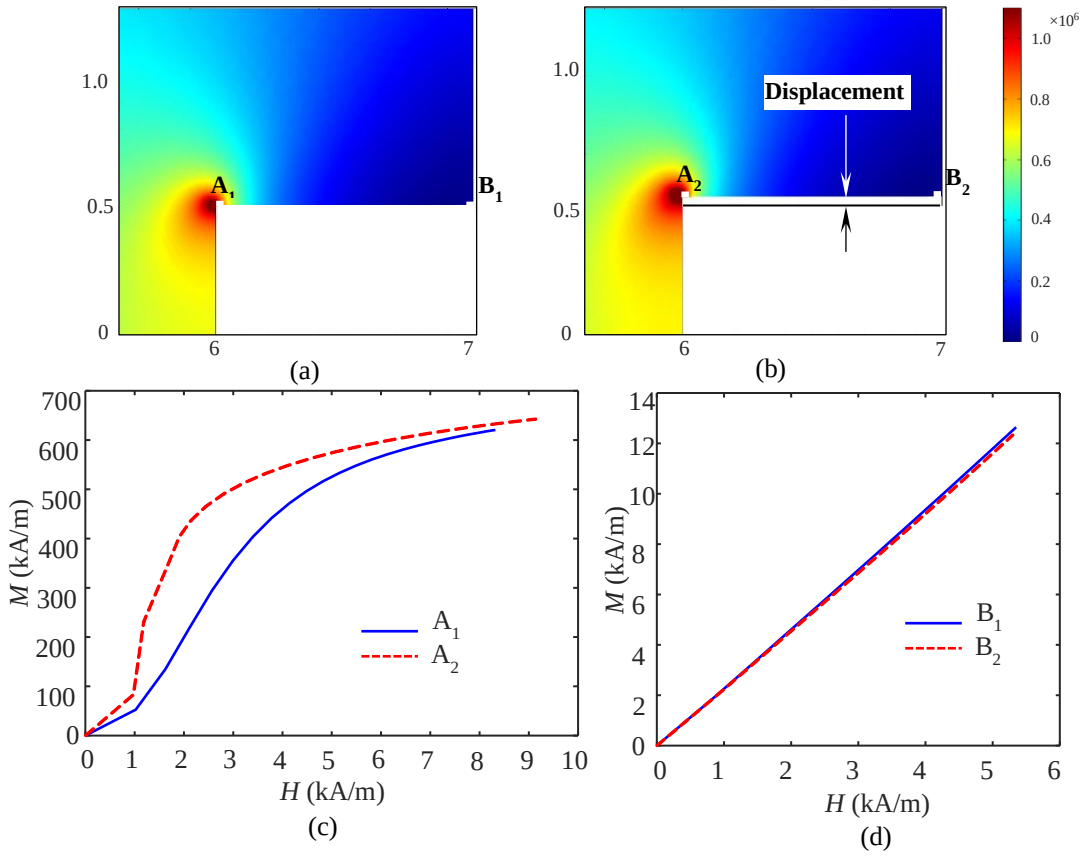

Fig. 3 Results of the magnetomechanical simulation. (a) Magnetization distribution without stress. (b) Magnetization distribution under 100 MPa tensile stress. (c) *M-H* curves extracted from points A_1 and A_2. (d) *M-H* curves extracted from points B_1 and B_2.

Fig. 3a and 3b show the simulation results at the final time step for the magnetization under stresses of 0 MPa and 100 MPa, respectively. To obtain these solutions, two complete *and separate* simulations were needed (for 0 MPa and for 100 MPa stresses) using the algorithm mentioned in Sections 2.1 and 2.2. It can be found that the magnetization changes significantly near the bottom of the defect, while varying only slightly near the top of the defect. To clearly illustrate the magnetization variations under different stresses, two characteristic points on each graph are selected. A_1, A_2, are surface points on the defect walls near the bottom of the square-notch, and B_1, B_2 are surface points near the top of the defect wall. Figure 3c shows the comparison of the *M-H* curves at points A_1 and A_2, while Fig.3d shows the comparison at points B_1 and B_2. It is obvious that the *M-H* curves at the points near the bottom of the defect change more dramatically than the points near the top. As shown in Fig.2d at 6.0mm distance (i.e.point A_2), the defect causes a significant stress concentration that is more than threefold with respect to the applied stress (340 MPa *vs.* 100 MPa), while at point B_2 the stress approaches zero. Despite an apparent closeness between the *M-H* curves at points B_1 and B_2 observed in Fig.3d, the values differ slightly and it does not overlap between those *M-H* curves. According to the dipole theory [4, 5], the magnetic flux leakage field of an off-surface point is influenced by the magnetization states of *all* points along the walls of the defect (e.g., segment A_1B_1), though the closer the elemental magnetic charge to the surface of the specimen, the greater is the effect on MFL. Such a great difference in magnetization values along the segment A_1B_1 also adds to the importance of the full scale problem simulation (avoiding any assumptions on the elemental magnetic charge distribution). The final time step magnetization results are used to calculate the MFL field with 1mm lift-off that is consistent with experiments. The MFL fields under different stresses are shown in Fig.5b and will be discussed later in Section 4.

3. Experimental details

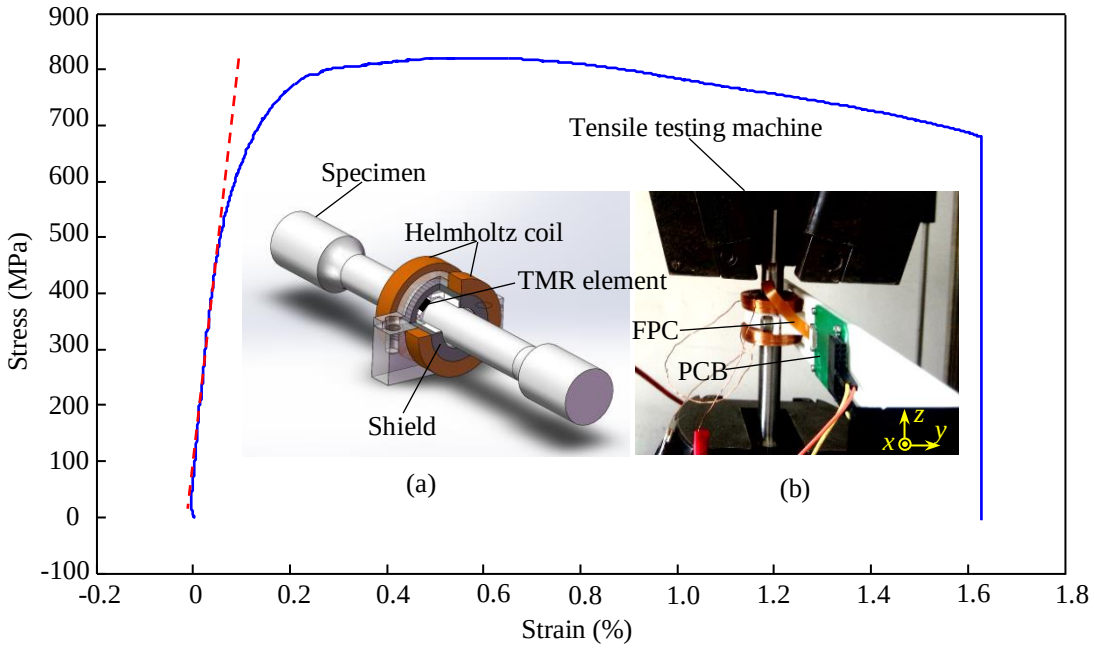

Fig. 4 Measured stress-strain curve of the 1045 steel. Inset (a) sketches a prototype of the TMR-based MFL sensor; inset (b) shows the experimental setup to measure the surface MFL induced by the defect on tensile test specimen.

Verification experiments are conducted on a specimen of 1045 steel. The physical dimensions and the chemical compositions of the specimen are listed in Table 1 and Table 3, respectively. According to the measured stress-strain curve (Fig.4) and stress concentration curve (Fig.2d), the tensile stress applied to the specimens in the following experiments is selected to be lower than 100MPa to ensure that the specimen remains in the elastic deformation region.

Table 3. Chemical compositions of the 1045 steel (wt. %, with the rest being Fe).

C	Si	Mn	P	S	Cr	Ni	Cu
0.42-0.50	0.17-0.37	0.50-0.80	0.035	0.035	0.25	0.25	0.25

A circumferential square-notch defect with both width and depth of 1 mm is machined on the surface of the centre of the "Reduced section" as shown in Fig.2a. A Helmholtz coil with magnetic shielding is used to provide a static magnetizing field with near-zero background field along the tensile direction of the specimen (Fig.4a). The tunnel-magnetoresistance (TMR) sensor together with its power supply circuit are mounted onto a linear guide rail. The location of the TMR sensor is concentric with the cylindrical specimen with a lift-off distance of 1 mm. The linear guide rail is driven by a step motor to enable the TMR device to scan the specimen surface at a speed of 10 mm/s. During scanning, the MFL-induced voltage signal $U(t)$ is acquired by a TektronixMDO3024 digital oscilloscope with a sampling rate of 100 S/s. The measured flux leakage intensity can be calculated using $H(t)=k_sU(t)$, where k_s is the sensitivity of the TMR- 8 mV/V/Oe (100 μV/V/A·m^{-1}) fitting in the range of ±50 Oe (±3978.87 A/m), which is lower than its specification, 12 mV/V/Oe (150μV/V/A·m^{-1}) in the field range of ±15 Oe (±1193.66 A/m), for this particular model. In the following experiments, the TMR sensor is supplied by 5 V power and used in differential mode doubling the output voltage. Hence, k_s is 1 mV/A·m^{-1} when the absolute value of the magnetic field is larger than 1193.66 A/m but lower than 3978.87 A/m.

Before the experiment, the specimen is annealed at 400°C for 2 h with furnace cooling to release the residual stress. As the simulation is conducted on the initial hysteresis stage, the specimen needs to be demagnetized before the test. Hence, a commercial demagnetization device is employed for specimen demagnetization. The surface magnetic field strength of the specimens is measured after the demagnetization process by a Gauss meter to make sure that the surface magnetic field strength is lower than 80 A/m. The exciting magnetic field is supplied by the Helmholtz coil, which is fed into 3 A current.

The experiments are carried out on the specimen with the circumferential square-notch defect and the MFL signals are detected by the TMR sensor with the specimen subjected to various stress levels. As mentioned above, in order to avoid plastic deformation in the defective zone, the stress applied to the specimen is limited to no more than 100 MPa. A stress increment of 10 MPa for data collection matches that used for the simulation steps. These experiments have been repeated five times to reduce measurement error.

4. Results and discussion

The simulated MFL results along the *z*-axis under zero stress are plotted in Fig.5a along with the experimentally recorded output voltage of the TMR sensor. At this final time step, the applied magnetic field is ~1592 A/m, and the sensitivity of the TMR sensor is 1 mV/A·m^{-1}. Therefore, the maximum output voltage of 0.7224 V (±0.02 V) just above the defect corresponds to a magnetic field intensity of 722.4 A/m (±20 A/m). For comparison, the simulated maximum value of the magnetic field is 748.78 A/m. In order to reduce the calculation error caused by demagnetization, lift-off and other factors, all experimental results and simulated curves are normalized to the maximum amplitude of the MFL signal under zero stress. As an example, the normalized results for 0 MPa, 50 MPa and 100 MPa

stresses are shown in Fig.5b. The simulation MFL shapes and highest amplitudes are consistent with the measured ones. It indicates that the proposed finite elemental simulation method is adequate to predict the stress-dependent MFL accurately in these conditions. The minimum value of the measured MFL signals on the left side of the defect are slightly lower than that of the simulation, while on the right side the opposite is seen. It may be caused by the slightly asymmetric shape of the defect due to the bevel angle of the machining tool.

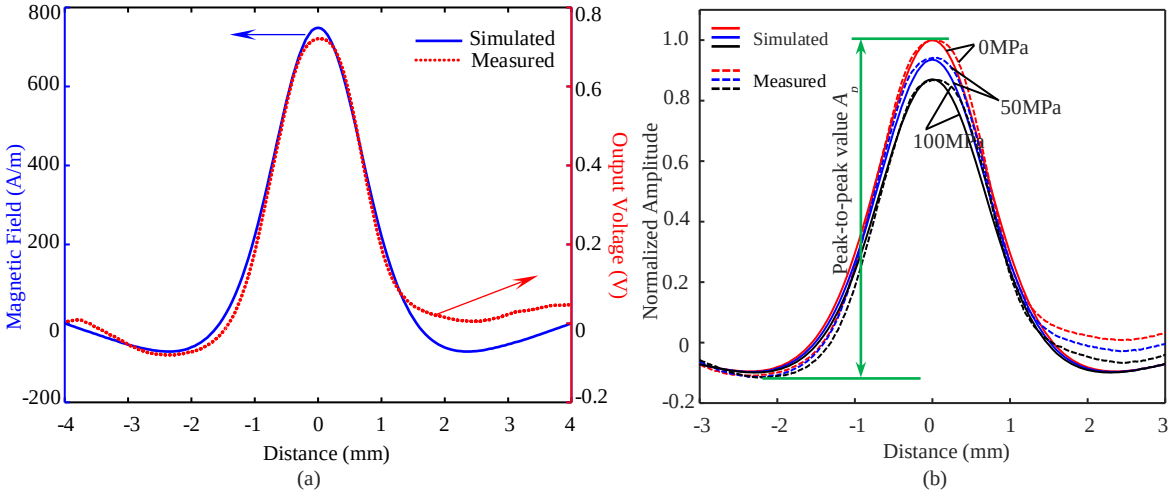

Fig. 5 (a) Simulation (solid lines) and experimental (dashed lines) results of the axial components of MFL along *z*-axis under 0MPa. (b) Normalized results of the axial components of MFL along *z*-axis under various stresses.

To evaluate the relationship between the MFL signal and the applied stress quantitatively, the peak-to-peak amplitudes A_p of normalized MFL signals are plotted in Fig.6. The dependence of the amplitude of the MFL signal on the applied stress obtained from experiment corresponds with the results obtained from simulation. The value of A_p demonstrates the approximately linear decreasing trend with increasing applied stress from 0 MPa to 100 MPa. This is due to the fact that the dominant stress along the defect wall is compressive stress that is increasing with applied stress. The linear equation fits well with the measured results with a coefficient of determination higher than 0.99.

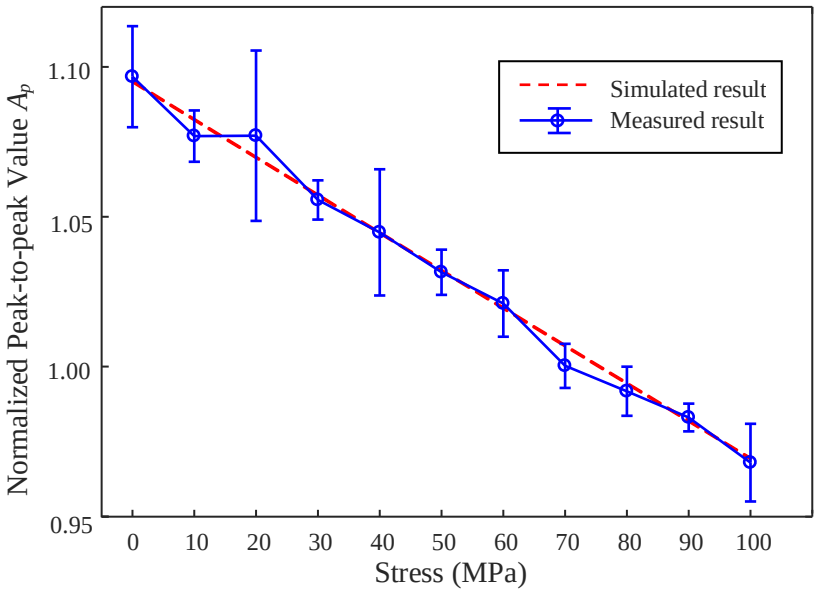

Fig. 6 Measured and simulated peak-to-peak amplitudes of the normalized MFL signals obtained from different stress conditions.

Applied tensile stress of 100 MPa results in an 11.76% decrease in the peak-to-peak amplitude of the MFL signals. Compared with our previous research [5], the absolute value of change is smaller, but it does not mean that the effect of stress can be omitted when defect dimensions are estimated. In this paper, the coupling finite elemental model is proposed to offer a method for solving the effect of stress on the MFL signal when the stress distribution around the defect is difficult to describe mathematically. Additionally, there may be defects with greater stress gradients distributed along the defect walls, resulting in a significantly greater influence on the profile of the MFL signal. Furthermore, if the material has higher relative permeability μ or a higher value of the magnetostriction coefficient b, the percentage change will be even bigger.

Several limitations of the proposed FEM model should be stated. Firstly, prior to any simulation, knowledge of certain specimen parameters is essential, including the J-A magnetomechanical model and spatial dimensions of the defect. As COMSOL uses an iterative method to solve the time-dependent problem, some parameters of the J-A model may result in nonconvergence, especially in the case of the magnetostriction coefficient b. If b is not selected properly, the model will not perform well since stresses on some elements may be beyond the limits of the J-A model. Secondly, in this model, the material is set as an isotropic steel and the model is simplified as a 2D axisymmetric structure. Anisotropic materials can be solved by assigning various values to different components of the tensors, but only directionally anisotropic problems may be solved rather than completely anisotropic. When solving anisotropic problems, the model should be built as a 3D structure, which might also face a nonconvergence error since the magnetization in an element is more complex than in the case of the isotropic problem. Thirdly, during the experiment, the speed of scanning may distort the profile of MFL signal due to eddy current effect. As the speed of the sensor was set to a relatively low value of 10mm/s in our experiments, the eddy current effect could be considered negligible here. In practical applications the scanning speed may be considerably faster and allowance for this velocity effect would need implementing using the method proposed in [28, 29].

5. Conclusion

A Multiphysics FEM method, which could deal with magnetomechanical problems, was proposed to simulate the MFL signal induced by a circumferential square-notch defect on a dog-bone shaped steel rod. The stress distribution of the specimen, especially the stress around the defect, was calculated in a solid mechanics module using a stationary solver. The results of the stress distribution were implemented as initial input values by the AC/DC magnetics module that was used to assess the distribution of stress-dependent magnetization in the specimen based on the magnetomechanical model. Finally, the MFL fields with 1 mm lift-off were extracted in postprocessing to predict the dependency of the peak-to-peak amplitudes of the MFL signal on applied stress.

Experimental work was conducted to obtain the variation trend of the MFL signal influenced by applied stress. The results from the measurements showed that the peak-to-peak value of MFL signal exhibited a decreasing trend with the action of increasing stress. It fitted the simulation results well. In this study, an increase in tensile stress of 100 MPa caused a decrease of 11.76% in the peak-to-peak amplitude of MFL signal. To size the defect accurately, the effect of stress on the MFL signal should be incorporated in the calibration process. The proposed multiphysics FEM model provides a valuable tool to evaluate the contribution of stress to the induced MFL signal and may be used to solve the inverse problem for sizing defects with a complicated stress distribution.

Acknowledgement

The authors thank Mr. Zengchong Yang and Donghang Wu from Beijing University of Technology for helping with the experimental work. This work was supported by the National Natural Science Foundation of China (Grant No. 11132002 and 11527801) and China Scholarship Council (CSC).

References

1. Wu, B., et al., *A novel TMR-based MFL sensor for steel wire rope inspection using the orthogonal test method.* Smart Materials and Structures, 2015. **24**(7).
2. Sun, Y.H., et al., *A Methodology for Identifying Defects in the Magnetic Flux Leakage Method and Suggestions for Standard Specimens.* Journal of Nondestructive Evaluation, 2015. **34**(3).
3. Mandal, K., et al., *Investigations of magnetic flux leakage and magnetic Barkhausen noise signals from pipeline steel.* Journal of Physics D-Applied Physics, 1997. **30**(6): p. 962-973.
4. Mandal, K. and D.L. Atherton, *A study of magnetic flux-leakage signals.* Journal of Physics D-Applied Physics, 1998. **31**(22): p. 3211-3217.
5. Wang, Y.J., et al., *Dipole modeling of stress-dependent magnetic flux leakage.* NDT & E International, 2018. **95**: p. 1-8.
6. Shcherbinin, N.Z.a.V., *Calculation of the magnetostatic field of surface defects. I. Field topography of defect models.* Defektoskopiya, 1966. **no.5**: p. 50-59.
7. Edwards, C. and S.B. Palmer, *The Magnetic Leakage Field of Surface-Breaking Cracks.* Journal of Physics D-Applied Physics, 1986. **19**(4): p. 657-673.
8. Hwang, J.H. and W. Lord, *Finite-Element Modeling of Magnetic Field Defect Interactions.* Journal of Testing and Evaluation, 1975. **3**(1): p. 21-25.
9. Atherton, D.L. and M.G. Daly, *Finite-Element Calculation of Magnetic-Flux Leakage Detector Signals.* NDT International, 1987. **20**(4): p. 235-238.
10. Altschuler, E. and A. Pignotti, *Nonlinear Model of Flaw Detection in Steel Pipes by Magnetic-Flux Leakage*. NDT & E International, 1995. **28**(1): p. 35-40.
11. Schifini, R. and A.C. Bruno, *Experimental verification of a finite element model used in a magnetic flux leakage inverse problem.* Journal of Physics D-Applied Physics, 2005. **38**(12): p. 1875-1880.
12. Ivanov, P.A., et al., *Magnetic flux leakage modeling for mechanical damage in transmission pipelines.* IEEE Transactions on Magnetics, 1998. **34**(5): p. 3020-3023.
13. Babbar, V., B. Shiari, and L. Clapham, *Mechanical damage detection with magnetic flux leakage tools: Modeling the effect of localized residual stresses.* IEEE Transactions on Magnetics, 2004. **40**(1): p. 43-49.
14. Babbar, V., J. Bryne, and L. Clapham, *Mechanical damage detection using magnetic flux leakage tools: modeling the effect of dent geometry and stresses.* NDT & E International, 2005. **38**(6): p. 471-477.
15. Zhong, L.Q., L.M. Li, and X. Chen, *Simulation of Magnetic Field Abnormalities Caused by Stress Concentrations.* IEEE Transactions on Magnetics, 2013. **49**(3): p. 1128-1134.
16. *https://uk.comsol.com/comsol-multiphysics*.
17. Sablik, M.J. and D.C. Jiles, *Coupled Magnetoelastic Theory of Magnetic and Magnetostrictive Hysteresis.* IEEE Transactions on Magnetics, 1993. **29**(4): p. 2113-2123.
18. Jiles, D.C., *Theory of the Magnetomechanical Effect.* Journal of Physics D-Applied Physics, 1995. **28**(8): p. 1537-1546.
19. Hubert, O. and S. Lazreg, *Two phase modeling of the influence of plastic strain on the magnetic and magnetostrictive behaviors of ferromagnetic materials.* Journal of Magnetism and Magnetic Materials, 2017. **424**: p. 421-442.
20. Bastos, J.o.P.A.a.o. and N. Sadowski, *Magnetic materials and 3D finite element modeling*. 2014, Boca Raton: CRC Press. xiii, 382 pages, 4 pages of unnumbered plates.
21. Bergqvist, A.J., *A simple vector generalization of the Jiles-Atherton model of hysteresis.* IEEE Transactions on Magnetics, 1996. **32**(5): p. 4213-4215.
22. Jiles, D.C. and D.L. Atherton, *Theory of the Magnetization Process in Ferromagnets and Its Application to the Magnetomechanical Effect.* Journal of Physics D-Applied Physics, 1984. **17**(6): p. 1265-1281.
23. Raghunathan, A., et al., *Generalized form of anhysteretic magnetization function for Jiles-Atherton theory of hysteresis.* Applied Physics Letters, 2009. **95**(17).
24. Liu, X.C.W., Y. J. , et al., *Design of Tunnel Magnetoresistive-Based Circular MFL Sensor Array for the Detection of Flaws in Steel Wire Rope.* Journal of Sensors, 2016.
25. LI, Z., et al., *Queries on the J-A Modeling Theory of the Magnetization Process in Ferromagnets and Proposed Correction Method.* Proceedings of the CSEE, 2011. **31**(3): p. 8.

26. Mierczak, L., *Evaluation of structural integrity of steel components by non-destructive magnetic methods*. PhD thesis, 2015, Cardiff University.
27. Mierczak, L., D.C. Jiles, and G. Fantoni, *A New Method for Evaluation of Mechanical Stress Using the Reciprocal Amplitude of Magnetic Barkhausen Noise.* IEEE Transactions on Magnetics, 2011. **47**(2): p. 459-465.
28. Li, Y., G.Y. Tian, and S. Ward, *Numerical simulation on magnetic flux leakage evaluation at high speed.* NDT & E International, 2006. **39**(5): p. 367-373.
29. Zhang, L.T., et al., *Influence of Specimen Velocity on the Leakage Signal in Magnetic Flux Leakage Type Nondestructive Testing.* Journal of Nondestructive Evaluation, 2015. **34**(2).